Designing plasmonic exceptional points by transformation optics

Zhu, Xinghong; Wang, Hongfei; Lei, Dangyuan; Pendry, J. B.; Li, Jensen

Designing plasmonic exceptional points by transformation optics

Xinghong Zhu,[1] Hongfei Wang,[2] Dangyuan Lei,[2] J. B. Pendry,[3] and Jensen Li[1,*]

[1]*Department of Physics, The Hong Kong University of Science and Technology, Clear Water Bay, Kowloon, Hong Kong, China*
[2]*Department of Materials Science and Engineering, City University of Hong Kong, 83 Tat Chee Avenue, Kowloon, Hong Kong, China*
[3]*The Blackett Laboratory, Department of Physics, Imperial College London, London SW7 2AZ, United Kingdom*
[*]*jensenli@ust.hk*

Abstract: Exceptional points (EPs) have been shown to be useful in bringing about sensitive optical properties based on non-Hermitian physics. For example, they have been applied in plasmonics to realize nano-sensing with extreme sensitivity. While the exceptional points are conventionally constructed by considering parity-time symmetric or anti-parity-time symmetric media, we theoretically demonstrate the possibility of generating a series of non-Hermitian systems by transforming a seed system with conventional parity-time symmetry within the transformation optics framework. The transformed systems do not possess PT-symmetry with a conventional parity operator after a spatial operation, i.e. hidden from conventional sense, but are equipped with exceptional points and phase transitions, hinting an alternative method to design non-Hermitian plasmonic systems with sensitive spectra or eigenmodes.

1. Introduction

Non-Hermitian optical systems have attracted a lot of attention due to their ability to generate sensitive optical properties around the so-called exceptional points [1–5]. A range of exotic wave phenomena have been demonstrated, ranging from unidirectional invisibility [6], spontaneous PT-symmetry breaking [7,8], coherent perfect absorption and lasing [9–11], etc. In particular, the sensitive optical properties around exceptional points, also an associated phase transition, can be very useful for sensing [12–14], mode discrimination (e.g. for lasing) [15–17] and isolation (non-reciprocal transmission) [18–20]. Recently, exceptional points have been successfully demonstrated in the optical regime, allowing the realization of exceptional point-based devices, such as ultrasensitive plasmonic sensors [21,22], and vortex beam generators [23]. In this case, the gain and loss are not merely compensating each other (e.g., active plasmonic systems [24,25]). The coupling and the gain-loss contrast between two different spatial domains interplay with each other and induce an exceptional point, in which both the eigenvalues and eigenvectors coalesce.

It is not trivial to guarantee the appearance of such an exceptional point for a generally non-Hermitian system [26]. One possible way is to impose a symmetry between two spatial domains through Parity-time (PT) operation on the material parameters [27–29]. The exceptional point can then be swept across configurationally by varying a single parameter (the ratio between coupling and gain-loss contrast). There are alternative routes, such as employing bianisotropy [30,31], considering anti-PT symmetry [32–38] and pseudo-Hermiticity [39,40], to construct non-Hermitian exceptional points. It is worth to mention that employing anti-PT symmetry to construct EPs is a relatively recent approach. EPs in these anti-PT systems have been found to enhance Sagnac effect in ring laser gyroscopes [34,35], in coupled waveguides with lossy buffers for on chip applications [36] and in side-coupled cavities for robust sensing [37] or

electromagnetically induced transparency [38]. The conventional P-symmetry can therefore be replaced by other kinds of symmetries. This work, in the same spirit of this route, investigates how transformation optics (TO) can help generate exceptional points by coordinate-transforming a known PT-symmetric system. We apply TO on a conventional PT-symmetric system and generate different daughter systems. Since the coordinate transformation does not preserve the original PT symmetry, the transformed daughter systems will not possess PT-symmetry with a conventionally defined parity operator, but are still equipped with exceptional points and phase transitions. In other words, the P-operation is effectively coordinate transformed while the T-operation stays the same. This approach is different from a previous scheme that employs a complex coordinate transformation to obtain a PT-symmetric system without phase transition from a lossless system [41,42]. TO has been previously used to design plasmonic systems with hidden symmetries, evolving from the earlier applications on designing invisibility cloaks to specific optical components [43–47]. For example, a broadband resonance can be hidden in a finite plasmonic structure with a singular geometry, with applications in nanofocusing, biosensing, energy harvesting, electron-energy loss spectroscopy, and strong coupling [48–57]. A third spatial dimension can be compacted and hidden into a two-dimensional plasmonic structure [58]. In the current case, the PT-symmetry is effectively hidden by the coordinate transformation without a conventionally defined P-operator (inversion or mirror) as a result of the TO approach.

2. Transformation optics applied on a PT-symmetric system

To illustrate the idea of TO in generating non-Hermitian systems with exceptional points, we start from a seed PT-symmetric plasmonic metal-insulator-metal (MIM) structure [59]. Figure 1(a) shows the MIM structure in complex coordinate $w = u + iv$. It comprises a thin slab of insulator of thickness d with permittivity $\epsilon_0 = 1$ (white, chosen as air) sandwiched by a lossy semi-infinite metal slab (blue) with permittivity $\epsilon_L = \epsilon + i\gamma$ ($\epsilon < 0$, $\gamma \geq 0$) for $u < -d/2$ and a semi-infinite gain material (orange) with permittivity $\epsilon_R = \epsilon - i\gamma$ for $u > d/2$. The system is parity-time symmetric, with parity being the mirror operation in u-direction, satisfying $\epsilon_L = \epsilon_R^*$ [60]. Now, we apply an exponential conformal map [61]

$$z = ge^{-\frac{2\pi w}{H}}, \tag{1}$$

which transforms the MIM system in coordinate w to concentric shells in coordinate $z = x + iy$, as shown in Fig. 1(b). We note that complex coordinates w and z are introduced as a compact notation for u, v and x, y which are the actual Cartesian coordinates, for simplicity in expressing conformal maps.

According to TO [43,48], the permittivity and permeability of the transformed structure ε', μ' are given by $\varepsilon' = \Lambda\varepsilon\Lambda^{\mathrm{T}}/(\det\Lambda)$, $\mu' = \Lambda\mu\Lambda^{\mathrm{T}}/(\det\Lambda)$, where Λ is the Jacobian transformation matrix:

$$\Lambda = \frac{2g\pi}{H}e^{-\frac{2\pi u}{H}}\begin{pmatrix} -\cos(2\pi v/H) & -\sin(2\pi v/H) & 0 \\ \sin(2\pi v/H) & -\cos(2\pi v/H) & 0 \\ 0 & 0 & He^{\frac{2\pi u}{H}}/(2g\pi) \end{pmatrix},$$

with $\det\Lambda = |dz/dw|^2$. For the plasmonic modes, we only need to consider TM (transverse magnetic) modes, in-plane components of the permittivity (index 1 and 2 in row and column) and out-of-plane component of the permeability tensors (index 3 in row and column). For a conformal map, by substituting the Jacobian into the transformation rule of permittivity and permeability, the transformed permittivity is found to be isotropic and is the same as the mother structures at corresponding mapped locations. The permeability, on the other hand, has its value changed according to the transformation rule. In our current case, we consider the near-field limit (wavelength much larger than the insulator thickness d and the size of the shells) while the
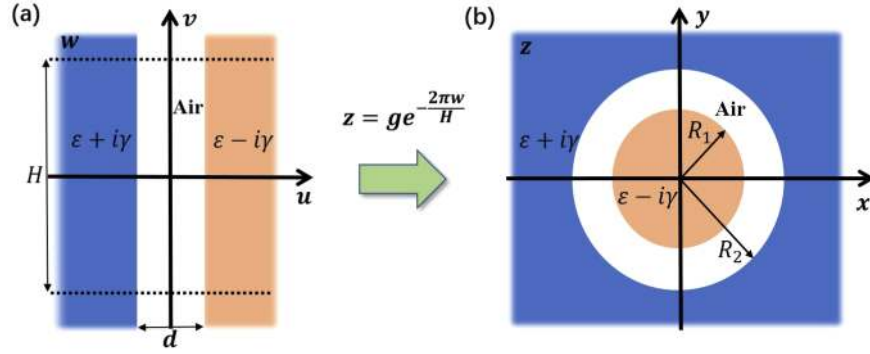
Fig. 1. Coordinate transformation from a mother metal-insulator-metal (MIM) structure in complex coordinate w (a) to concentric shells in complex coordinate z (b). In (a) the MIM structure is a well-defined PT-symmetric system. The blue (Orange) slab has a permittivity $\epsilon + i\gamma$ ($\epsilon - i\gamma$) in loss (gain), and the white area represents an insulator slab with unit permittivity. In (b), the daughter system consists of the same materials (represented with the same colours) in cylindrical shells.

effect of retardation will be considered in a later step. In this limit, the transformed permeability is neglected [62]. As a result of the transformation, the lossy slab becomes the area (in blue, with permittivity $\epsilon + i\gamma$) outside a cylindrical area of radius R_2. The slab with gain becomes the cylinder (in orange, with permittivity $\epsilon - i\gamma$) with radius R_1. The thin shell in white colour is the air with unit permittivity. The parameter g controls the sizes of the transformed cylinders. The transformed shells have radii R_1 and R_2 governed by $R_1 e^{\pi d/H} = R_2 e^{-\pi d/H} = g$, where H is the period of the slab system, artificially imposed in the v direction. H is chosen according to the ratio between R_1 and R_2 while both R_1 and R_2 should be small compared with the wavelength. The system in physical coordinate (x and y) can now be regarded as equivalent to the PT-symmetric system in the virtual coordinate (u and v) but without conventional sense of PT-symmetry, i.e., without an obvious definition of the P-operation after transformation.

A local plasmon mode on the w-plane, is the so-called gap plasmon [59,63] with transverse-magnetic (TM) polarization, satisfying in the near-field limit:

$$e^{\frac{4\pi m d}{H}} = \left(\frac{\epsilon_L - 1}{\epsilon_L + 1}\right)\left(\frac{\epsilon_R - 1}{\epsilon_R + 1}\right), \tag{2}$$

where m, a positive integer, corresponds to discretized linear momentum due to the imposed period H in the w-plane. According to TO, the same equation also describes the mode spectra in the z-plane when the wavelength is much larger than sizes of the shells (R_2) and the thickness of insulator (d). Then m corresponds to the angular momentum of a TM mode ((E_x, E_y, H_z) with $H_z \propto \exp(im \arg z)$) in the z-plane.

Here, we set $d = 20.0$ nm, $R_1 = 3.3$ nm, and $R_2 = 13.3$ nm as the geometric parameters of the current example. With $\epsilon_L = \epsilon + i\gamma$ and $\epsilon_R = \epsilon - i\gamma$, we can obtain the local plasmon dispersion (over ϵ and γ, as shown in Fig. 2(a)) for the MIM system using full-wave simulations (COMSOL Multiphysics). In the simulation, the system is excited by an array of dipoles pointing in the u-direction at a wavelength of 600 nm, periodically placed in the v-direction with period H. The colour profile plots the averaged field intensity over the metal/dielectric surfaces (where the local plasmon modes localize) in log scale with red colour (high intensity) indicates the local plasmon mode dispersion obtained numerically. The two $m = 1$ modes start with $\epsilon = -1.73$ and $\epsilon = -0.6$ at $\gamma = 0$. Then the splitting between the two modes becomes smaller when γ increases until a certain point at $\gamma \cong 0.55$ at which the two $m = 1$ modes become degenerate. The $m = 2$ modes
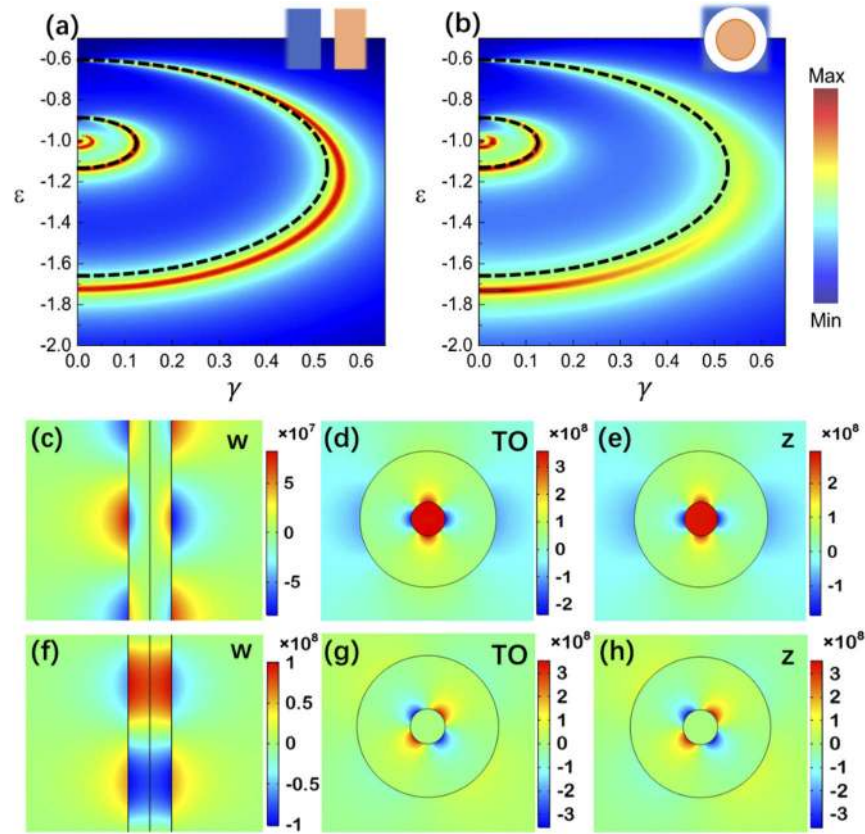
Fig. 2. Local plasmon condition in terms of ϵ and γ (the real and imaginary parts of the permittivities) for the MIM system in w-plane (a) and for the cylindrical shells in the z-plane (b). The colour map shows the average of $|E_x|^2$ over the metal/dielectric interface (in log scale). The red colour shows the locations with highest E-field intensity, i.e. the local plasmon condition. The dashed line in both (a) and (b) shows the local plasmon condition by solving ϵ from Eq. (2) with varying γ. $m = 1$ (the larger parabola) and $m = 2$ (the smaller parabola) are the two plasmon conditions in the near-field limit. The geometric parameters are $d = 20.0$ nm, $R_1 = 3.3$ nm, and $R_2 = 13.3$ nm. The conformal map in Eq. (1) has parameters $g = 6.6$ nm and $H = 90.0$ nm. (c) gap plasmon mode (showing only E_x distribution) at $\gamma = 0.02, \epsilon = -0.6$ in the w plane and its coordinate transformation result (d) (showing only in E_x distribution). (e) E_x distribution obtained using a dipole excitation directly in the cylindrical z plane at $\gamma = 0.02, \epsilon = -0.6$. (f) gap plasmon mode (showing only E_x distribution) at $\gamma = 0.02, \epsilon = -1.73$ in the w plane and its coordinate transformation result (g) (showing only in E_x distribution). (h) E_x distribution obtained using a dipole excitation directly in the cylindrical z plane at $\gamma = 0.02, \epsilon = -1.73$.

show up as a smaller "parabola," while the $m = 3$ modes appear as an even smaller one around the point $\epsilon = -1$ and $\gamma = 0$ (the higher-order modes are not clearly resolved around the same point). In Fig. 2(b), the dispersion diagram is solved by full-wave simulations in the x-y plane (Fig. 1(b)) using a dipole excitation pointing along the x-direction at $(g, 0)$ [48]. The two dispersions exhibit a similar permittivity dependence, confirming the equivalence between the two systems for the mode spectra. It should be noted that different points in the color map represent different systems with fixed wavelength excitation in the full wave simulation in principle. However, one can substitute a frequency dispersion, e.g., the Drude model of permittivity into Eq. (2) and solve for

k_0 to get distinct modes of a single system at any specific γ (see later Fig. 3). In order to have an intuitive sense of the equivalence, Fig. 2(c) and (f) shows the E_x-field profile for the gap plasmon mode $\gamma = 0.02$, $\epsilon = -0.6$(odd mode for E_x) and $\gamma = 0.02$, $\epsilon = -1.73$ (even mode for E_x) in the w plane and the field fits one wavelength in a period H in the vertical direction. We transform this field to the z plane by the coordinate transformation according to TO [50] and the TO-transformed field (again only showing E_x profile) is plot in Fig. 2(d) and (g). The transformed field shows a very similar quality to the result in Fig. 2(e) and (h), which is directly excited in the cylindrical z plane. We note that the equivalence is not exact as there are approximations here. The permeability μ is kept at value 1 for the whole domain in both w-plane and z-plane in the near-field limit. For TO theory, the permeability μ becomes inhomogeneous in the transformed z-plane, as discussed above. The near-field approximation becomes more accurate only when the wavelength is much larger than the sizes of the cylinders [64]. In the present case, the wavelength is sufficiently large to ensure the equivalence between the two domains. On the other hand, the retardation effect shows up by plotting the analytic mode dispersions obtained from Eq. (2) (solving for ϵ by varying γ). The analytic mode dispersions are plotted in the two panels of Fig. 2 as dashed lines for both $m = 1$ and $m = 2$ modes. The size of the $m = 1$ "parabola" has a small mismatch with the colour map in Fig. 2(a) and (b) due to the retardation effect. Nonetheless, we can conclude that the two systems have very similar mode dispersions (confirmed by the full-wave simulations). The system in the z-plane, although lacking a well-defined PT-symmetry, has an origin from the system in the w-plane, which is purposely designed to be conventional PT-symmetric. In the dispersion relation of $m = 1$, when the two branches become degenerate at around $\gamma \cong 0.55$, such a non-Hermitian system exhibits an exceptional point, which will be investigated in the next section. We note that the mode in the broken phase (with γ beyond the exceptional point) is not showing up in Fig. 2 as the full-wave simulations (color map) are performed with a point source excitation with only a real value of ϵ, while the mode in the broken phase has an imaginary ϵ in solving the mode equation.
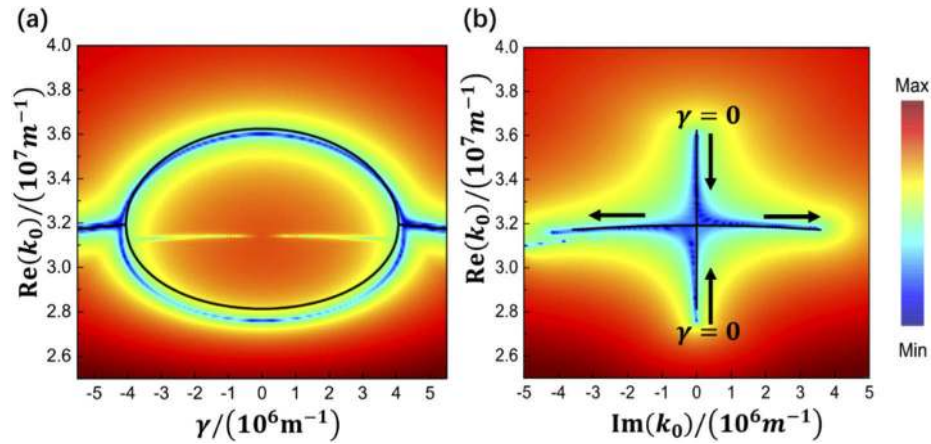
Fig. 3. Exceptional point dynamics. The complex wavenumber k_0 satisfying the mode equation with retardation effect is plotted against the gain-loss contrast γ (according to Drude model (Eq. (9)) in (a) $Re(k_0)$ against γ and in (b) trajectory of complex k_0 when γ increases from zero to $5.5 \times 10^6 \text{m}^{-1}$. The solid black lines are the theoretical results by plugging in Drude model into Eq. (2) without considering retardation effect. The sizes of the cylinders are scaled down by 50% with parameters listed in the caption of Fig. 2.

3. Hidden PT-symmetry with exceptional point dynamics

The above discussion assumes the near-field limit and solves for ϵ from the mode equation (Eq. (2)) in the w-plane by substituting $\epsilon_L = \epsilon + i\gamma$ and $\epsilon_R = \epsilon - i\gamma$ for the analytic solution. The same mode equation can be mathematically recast as an eigenvalue problem for the MIM structure:

$$(\mathcal{H} - \epsilon I)\begin{pmatrix} E_v(-d/2) \\ E_v(+d/2) \end{pmatrix} = 0, \tag{3}$$

where the 2×2 Hamiltonian is governed by

$$\mathcal{H} = \begin{pmatrix} -\frac{\xi^{2m}+1}{\xi^{2m}-1} - i\gamma & \frac{2\xi^m}{\xi^{2m}-1} \\ \frac{2\xi^m}{\xi^{2m}-1} & -\frac{\xi^{2m}+1}{\xi^{2m}-1} + i\gamma \end{pmatrix}, \tag{4}$$

with $\xi = \exp(2\pi d/H)$ and eigenvalue ϵ to give the same secular equation (Eq. (2)). $E_v(\mp d/2)$ is the electric field in the vertical v-direction at $u = -d/2$ and $d/2$. The Hamiltonian $\mathcal{H}$ can be directly related to a 2×2 PT-symmetric Hamiltonian, with the P-operation as the mirror operation in the u-direction and T being the time-reversal operation in this case [27–29]. The two eigenvalues become either two real numbers or a complex conjugate pair. Figure 2 captures the symmetric phase when the two eigenvalues ϵ are real up to the exceptional point (e.g., $\gamma \cong 0.55$ for $m = 1$ mode). $\epsilon_R = \epsilon_L^*$ is now regarded as the hidden PT-symmetry (i.e. without conventional identification of PT operation) condition in the near-field limit in the z-plane. The TO allows us to replace $\xi \to R_2/R_1$, $E_v(-d/2) \to -2\pi R_2 E_\phi(R_2)/H$, $E_v(d/2) \to -2\pi R_1 E_\phi(R_1)/H$ and the corresponding eigenvalue problem in the z-plane becomes

$$A\begin{pmatrix} R_2 E_\phi(R_2) \\ R_1 E_\phi(R_1) \end{pmatrix} = (\mathcal{H} - \epsilon I)\begin{pmatrix} R_2 E_\phi(R_2) \\ R_1 E_\phi(R_1) \end{pmatrix} = 0, \tag{5}$$

where E_ϕ is the electric field in the azimuthal direction. We note that the P-operation in the matrix level is still identified as the application of matrix {{0,1},{1,0}} while the T-operation is conjugate operation. However, in the field solution level, the P operation is not the conventional one. It is transformed by the mapping from $u \leftrightarrow -u$ to $r \leftrightarrow g^2/r$ as the new meaning, according to the conformal mapping Eq. (1).

After making the PT-symmetry origin clear in both materials profile (PT-symmetric in w-plane) and the abstract mathematical equivalence (Eq. (5)), we now incorporate the retardation effect. The consideration of the retardation effect is necessary if we want to solve for eigen-frequency (equivalently finite wavenumber $k_0 = \omega/c$) directly and observe the dynamics of exceptional point in the complex frequency plane. By adding δA, a function of k_0, ϵ_L and ϵ_R and can be seen as a perturbation term for a small k_0, the mode equation is then the solution of $\det(A + \delta A) = 0$. The mode equation ($m = 1$) with retardation effect can be written as

$$R_2^2(\epsilon_L + 1)(\epsilon_R + 1) - R_1^2(\epsilon_L - 1)(\epsilon_R - 1) + \delta f(k_0, \epsilon_L, \epsilon_R) = 0, \tag{6}$$

where

$$\delta f = (R_2^2 - R_1^2)\text{Tr}\left(\begin{pmatrix} 0 & 1 \\ -1 & 0 \end{pmatrix} A \begin{pmatrix} 0 & -1 \\ 1 & 0 \end{pmatrix} (\delta A)^T\right), \tag{7}$$

represents a perturbation of the mode equation introduced by the retardation effect. Tr and superscript T mean the trace and transpose of a matrix. In this case, Eq. (6) is generally complex.

To restore the case of PT-symmetry that only one scanning parameter is needed to get an EP, we perturb the hidden PT-symmetry condition (imaginary part of l.h.s. of Eq. (6) now stays zero) by

$$\epsilon_R = \epsilon_L^* - \frac{i\mathrm{Im}\delta f(k_0, \epsilon_L, \epsilon_L^*)}{R_2^2 + R_1^2 + (R_2^2 - R_1^2)\epsilon_L}, \tag{8}$$

it will be possible to capture the exceptional point by scanning γ, the gain-loss contrast. In the near field limit, $\delta f \to 0$, the hidden PT-symmetry condition returns to $\epsilon_R = \epsilon_L^*$. The modified condition (Eq. (8)) thus allows us to have a correction due to a finite k_0 (δf depends on k_0) and to observe the exceptional point dynamics in the complex frequency plane.

We note that Eq. (8) (derived from the perturbation theory) is only quantitatively accurate for small frequencies, or equivalently at small sizes of the cylinders compared to the free-space wavelength. As an example, we scale down the physical sizes of the cylinders by half. The ϵ_L and ϵ_L^* in Eqs. (6) and (8) are now replaced by a frequency-dispersive Drude model:

$$\epsilon_L \to 1 - \frac{k_p^2}{k_0^2 + 2ik_0\gamma}, \quad \epsilon_L^* \to 1 - \frac{k_p^2}{k_0^2 - 2ik_0\gamma}, \tag{9}$$

where the plasma wavenumber k_p is set at $2\pi/137$ nm (for silver) [65]. Figure 3(a) plots the magnitude of l.h.s of the mode equation with retardation effect (Eq. (6)), with low intensity (blue) indicating the $m = 1$ mode, i.e. showing the solved k_0 by varying γ. The splitting between the two modes of purely real k_0 at $\gamma = 0$ decreases as γ increases, and the two modes then become degenerate at $|\gamma| \cong 4.2 \times 10^6 \mathrm{m}^{-1}$ (i.e. at an exceptional point). The dynamics in approaching the exceptional point can be illustrated by plotting the trajectory of the complex k_0 when we increase γ from 0 to $5.5 \times 10^6 \mathrm{m}^{-1}$, as shown in Fig. 3(b). Compared with the theoretical results (by substituting Eq. (8) and Eq. (9) into Eq. (2) without the retardation term) of exceptional point dynamics without considering retardation effect shown in solid black lines, we can see that the retardation effect will shift the local plasmon condition and the exceptional point a little bit. The two modes with purely real k_0 merge at around $k_0 \cong 3.2 \times 10^7 \mathrm{m}^{-1}$ and then become a complex conjugate pair when γ further increases (roughly forming a bending of 90 degrees). This behaviour is similar to a conventional PT-symmetric system, except the fact that the PT-symmetry is hidden in the cylindrical domain where the P-operator cannot be defined as a conventional mirror or inversion operation. The EP is also about a nonlinear eigenvalue problem [66].

4. Generating other hidden PT-symmetric systems

From the above discussion, TO serves as a guidance in obtaining non-Hermitian systems that can capture exceptional points, with an origin from a conventional PT-symmetric system. In fact, we can adopt other maps from the virtual space (w-plane) to obtain and generate other non-Hermitian systems with hidden PT-symmetries. In the current case, we further cascade a Mobius map $z = g(a + w)/(b - w)$ so that the metal cylinder with gain can be shifted from its current position (shown in Fig. 4(a)). There is a shift in distance d from the center of the lossy shell in the z-plane. As an example, we set $R_1 = 3.1$ nm, $R_2 = 14.6$ nm and $d = 5.5$ nm. The resultant dispersion diagram (full-wave simulations shown as the colour map) is shown in Fig. 4(b). For the concentric structure, the dispersion relation with retardation effect in Fig. 2(b) is plotted as the dashed lines for the fundamental and second modes. It is found to have a good agreement with the colour map. Therefore, the non-concentric system shown in Fig. 4(a) is also having a hidden PT-symmetry.
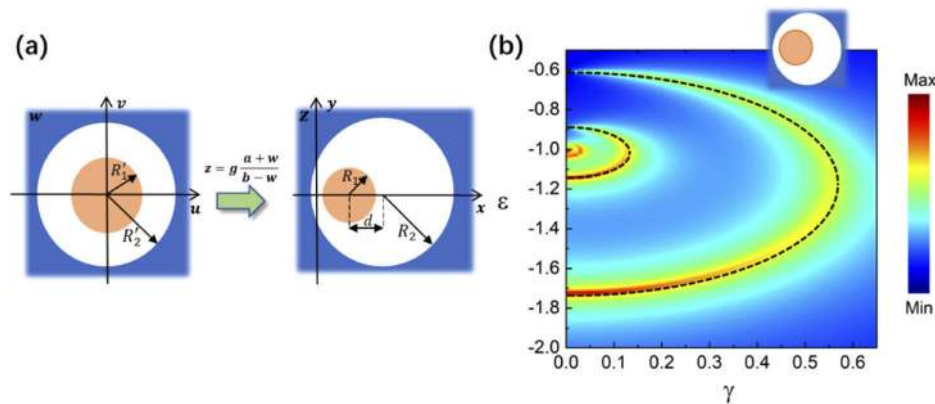
Fig. 4. (a). A mobius transformation $z = g(a + w)(b - w)$ converts concentric shell structure with loss (blue region $\epsilon + i\gamma$) and gain (orange region $\epsilon - i\gamma$) into a non-concentric structure with lossy cylinder shell enclosing a gain cylinder. The mapping has parameters $a = 6.6$ nm, $b = 33.4$ nm, $g = 25.8$ nm. The geometric parameters in the w-plane are the same as those in Fig. 1(b). The radius of the gain cylinder and lossy shell in the z plane are $R_1 = 3.1$ nm, $R_2 = 14.6$ nm. The centre of the gain cylinder is displaced by $d = 5.5$ nm from the centre of the lossy shell. (b) Local plasmon dispersions of a non-concentric structure in terms of ϵ and γ (the real and imaginary parts of the permittivities). The dashed lines are simulated fundamental and second modes of concentric structure with retardation effect in Fig. 2(b). The colour map shows the average of $|E_x|^2$ in logscale over the metal/dielectric interface.

5. Conclusion

We have established a generic approach to construct various non-Hermitian systems with exceptional points through coordinate transformations. We have applied this approach to transform a conventional PT-symmetric system, a plasmonic MIM structure, to generate systems with hidden PT-symmetry. The same approach can also be equivalently applied to systems (other than the MIM structure) with other origins of exceptional points, such as anti-PT symmetric or bianisotropic systems. The investigations will be useful for exceptional point-based sensing, lasing, and generally for non-Hermitian plasmonics.

Disclosures. The authors declare no conflicts of interest.

References

1. W. D. Heiss, "Repulsion of resonance states and exceptional points," Phys. Rev. E **61**(1), 929–932 (2000).
2. M. V. Berry, "Physics of nonhermitian degeneracies," Czech. J. Phys. **54**(10), 1039–1047 (2004).
3. S. B. Lee, J. Yang, S. Moon, S. Y. Lee, J. B. Shim, S. W. Kim, J. H. Lee, and K. An, "Observation of an Exceptional Point in a Chaotic Optical Microcavity," Phys. Rev. Lett. **103**(13), 134101 (2009).
4. W. D. Heiss, "The physics of exceptional points," J. Phys. A: Math. Theor. **45**(44), 444016 (2012).
5. B. Zhen, C. W. Hsu, Y. Igarashi, L. Lu, I. Kaminer, A. Pick, S. L. Chua, JD. Joannopoulos, and M. Soljačić, "Spawning rings of exceptional points out of Dirac cones," Nature **525**(7569), 354–358 (2015).
6. A. Regensburger, C. Bersch, M. A. Miri, G. Onishchukov, D. N. Christodoulides, and U. Peschel, "Parity–time synthetic photonic lattices," Nature **488**(7410), 167–171 (2012).
7. C. E. Rüter, K. G. Makris, R. El-Ganainy, D. N. Christodoulides, M. Segev, and D. Kip, "Observation of parity–time symmetry in optics," Nat. Phys. **6**(3), 192–195 (2010).
8. A. Guo, G. J. Salamo, D. Duchesne, R. Morandotti, M. Volatier-Ravat, V. Aimez, G. A. Siviloglou, and D. N. Christodoulides, "Observation of P T-symmetry breaking in complex optical potentials," Phys. Rev. Lett. **103**(9), 093902 (2009).
9. S. Longhi, "PT-symmetric laser absorber," Phys. Rev. A **82**(3), 031801 (2010).

10. Y. D. Chong, Li Ge, and A. Douglas Stone, "PT-symmetry breaking and laser-absorber modes in optical scattering systems," Phys. Rev. Lett. **106**(9), 093902 (2011).

11. Y. Fu, Y. Xu, H. Chen, and S. A. Cummer, "Coherent perfect absorption and laser modes in a cylindrical structure of conjugate metamaterials," New J. Phys. **20**(1), 013015 (2018).

12. W. Chen, Ş. K. Özdemir, G. Zhao, J. Wiersig, and L. Yang, "Exceptional points enhance sensing in an optical microcavity," Nature **548**(7666), 192–196 (2017).

13. J. Wiersig, "Enhancing the sensitivity of frequency and energy splitting detection by using exceptional points: application to microcavity sensors for single-particle detection," Phys. Rev. Lett. **112**(20), 203901 (2014).

14. H. Hodaei, A. U. Hassan, S. Wittek, H. Garcia-Gracia, R. El-Ganainy, D. N. Christodoulides, and M. Khajavikhan, "Enhanced sensitivity at higher-order exceptional points," Nature **548**(7666), 187–191 (2017).

15. L. Feng, Z. J. Wong, R. M. Ma, Y. Wang, and X. Zhang, "Single-mode laser by parity-time symmetry breaking," Science **346**(6212), 972–975 (2014).

16. H. Hodaei, M. A. Miri, M. Heinrich, D. N. Christodoulides, and M. Khajavikhan, "Parity-time–symmetric microring lasers," Science **346**(6212), 975–978 (2014).

17. H. Alaeian and J. A. Dionne, "Controlling electric, magnetic, and chiral dipolar emission with PT-symmetric potentials," Phys. Rev. B **91**(24), 245108 (2015).

18. R. Thomas, H. Li, F. M. Ellis, and T. Kottos, "Giant nonreciprocity near exceptional-point degeneracies," Phys. Rev. A **94**(4), 043829 (2016).

19. Y. Choi, C. Hahn, J. W. Yoon, S. H. Song, and P. Berini, "Extremely broadband, on-chip optical nonreciprocity enabled by mimicking nonlinear anti-adiabatic quantum jumps near exceptional points," Nat. Commun. **8**(1), 1–9 (2017).

20. J. Wang, H. Y. Dong, Q. Y. Shi, W. Wang, and K. H. Fung, "Coalescence of nonreciprocal exceptional points in magnetized PT-symmetric systems," Phys. Rev. B **97**(1), 014428 (2018).

21. J. H. Park, A. Ndao, W. Cai, L. Hsu, A. Kodigala, T. Lepetit, Y. H. Lo, and B. Kanté, "Symmetry-breaking-induced plasmonic exceptional points and nanoscale sensing," Nat. Phys. **16**(4), 462–468 (2020).

22. A. Tuniz, T. Wieduwilt, and M. A. Schmidt, "Tuning the Effective P T Phase of Plasmonic Eigenmodes," Phys. Rev. Lett. **123**(21), 213903 (2019).

23. H. M. Leung, W. Gao, R. Zhang, Q. Zhao, X. Wang, C. T. Chan, J. Li, and W. Y. Tam, "Exceptional point-based plasmonic metasurfaces for vortex beam generation," Opt. Express **28**(1), 503–510 (2020).

24. J. Seidel, S. Grafström, and L. Eng, "Stimulated emission of surface plasmons at the interface between a silver film and an optically pumped dye solution," Phys. Rev. Lett. **94**(17), 177401 (2005).

25. I. DeLeon and P. Berini, "Amplification of long-range surface plasmons by a dipolar gain medium," Nat. Photonics **4**(6), 382–387 (2010).

26. H. Lourenço-Martins, P. Das, L.H. Tizei, R. Weil, and M. Kociak, "Self-hybridization within non-Hermitian localized plasmonic systems," Nat. Phys. **14**(4), 360–364 (2018).

27. C. M. Bender and S. Boettcher, "Real spectra in non-Hermitian Hamiltonians having P T symmetry," Phys. Rev. Lett. **80**(24), 5243–5246 (1998).

28. C. M. Bender, D. C. Brody, and H. F. Jones, "Complex extension of quantum mechanics," Phys. Rev. Lett. **89**(27), 270401 (2002).

29. C. M. Bender, "Making sense of non-Hermitian Hamiltonians," Rep. Prog. Phys. **70**(6), 947–1018 (2007).

30. J. Gear, F. Liu, S.T. Chu, S. Rotter, and J. Li, "Parity-time symmetry from stacking purely dielectric and magnetic slabs," Phys. Rev. A **91**(3), 033825 (2015).

31. J. Gear, Y. Sun, S. Xiao, L. Zhang, R. Fitzgerald, S. Rotter, H. Chen, and J. Li, "Unidirectional zero reflection as gauged parity-time symmetry," New J. Phys. **19**(12), 123041 (2017).

32. Y. Choi, C. Hahn, J. W. Yoon, and S. H. Song, "Observation of an anti-PT-symmetric exceptional point and energy-difference conserving dynamics in electrical circuit resonators," Nat. Commun. **9**(1), 1–6 (2018).

33. X. L. Zhang, T. Jiang, and C. T. Chan, "Dynamically encircling an exceptional point in anti-parity-time symmetric systems: asymmetric mode switching for symmetry-broken modes," Light: Sci. Appl. **8**(1), 1–9 (2019).

34. Y. H. Lai, Y. K. Lu, M. G. Suh, Z. Yuan, and K. Vahala, "Observation of the exceptional-point-enhanced Sagnac effect," Nature **576**(7785), 65–69 (2019).

35. M. P. Hokmabadi, A. Schumer, D. N. Christodoulides, and M. Khajavikhan, "Non-Hermitian ring laser gyroscopes with enhanced Sagnac sensitivity," Nature **576**(7785), 70–74 (2019).

36. H. Fan, J. Chen, Z. Zhao, J. Wen, and Y. P. Huang, "Antiparity-time symmetry in passive nanophotonics," ACS Photonics **7**(11), 3035–3041 (2020).

37. Q. Zhong, J. Ren, M. Khajavikhan, D. N. Christodoulides, Ş. K. Özdemir, and R. El-Ganainy, "Sensing with exceptional surfaces in order to combine sensitivity with robustness," Phys. Rev. Lett. **122**(15), 153902 (2019).

38. C. Wang, X. Jiang, G. Zhao, M. Zhang, C. W. Hsu, B. Peng, A. D. Stone, L. Jiang, and L. Yang, "Electromagnetically induced transparency," Nat. Phys. **16**(3), 334–340 (2020).

39. A. Mostafazadeh, "Pseudo-Hermiticity versus PT symmetry: the necessary condition for the reality of the spectrum of a non-Hermitian Hamiltonian," J. Math. Phys. **43**(1), 205–214 (2002).

40. X. Cui, K. Ding, J. W. Dong, and C. T. Chan, "Realization of complex conjugate media using non-PT-symmetric photonic crystals," Nanophotonics **9**(1), 195–203 (2019).

41. G. Castaldi, S. Savoia, V. Galdi, A. Alu, and N. Engheta, "PT metamaterials via complex-coordinate transformation optics," Phys. Rev. Lett. **110**(17), 173901 (2013).

42. S. Savoia, G. Castaldi, and V. Galdi, "Complex-coordinate non-Hermitian transformation optics," J. Opt. **18**(4), 044027 (2016).

43. J. B. Pendry, D. Schurig, and D. R. Smith, "Controlling electromagnetic fields," Science **312**(5781), 1780–1782 (2006).

44. U. Leonhardt, "Optical conformal mapping," Science **312**(5781), 1777–1780 (2006).

45. J. Li and J. B. Pendry, "Hiding under the carpet: a new strategy for cloaking," Phys. Rev. Lett. **101**(20), 203901 (2008).

46. H. Chen, B. Hou, S. Chen, X. Ao, W. Wen, and C. T. Chan, "Design and experimental realization of a broadband transformation media field rotator at microwave frequencies," Phys. Rev. Lett. **102**(18), 183903 (2009).

47. M. Rahm, D. Schurig, D. A. Roberts, S. A. Cummer, D. R. Smith, and J. B. Pendry, "Design of electromagnetic cloaks and concentrators using form-invariant coordinate transformations of Maxwell's equations," Phot. Nano. Fund. Appl. **6**(1), 87–95 (2008).

48. A. Aubry, D. Y. Lei, A. I. Fernández-Domínguez, Y. Sonnefraud, S. A. Maier, and J. B. Pendry, "Plasmonic light-harvesting devices over the whole visible spectrum," Nano Lett. **10**(7), 2574–2579 (2010).

49. A. Aubry, D. Y. Lei, S. A. Maier, and J. B. Pendry, "Broadband plasmonic device concentrating the energy at the nanoscale: The crescent-shaped cylinder," Phys. Rev. B **82**(12), 125430 (2010).

50. D. Y. Lei, A. Aubry, S. A. Maier, and J. B. Pendry, "Broadband nano-focusing of light using kissing nanowires," New J. Phys. **12**(9), 093030 (2010).

51. Y. Luo, D. Y. Lei, S. A. Maier, and J. B. Pendry, "Broadband light harvesting nanostructures robust to edge bluntness," Phys. Rev. Lett. **108**(2), 023901 (2012).

52. J. B. Pendry, A. Aubry, D. R. Smith, and S. A. Maier, "Transformation optics and subwavelength control of light," Science **337**(6094), 549–552 (2012).

53. J. B. Pendry, A. I. Fernández-Domínguez, Y. Luo, and R. Zhao, "Capturing photons with transformation optics," Nat. Phys. **9**(8), 518–522 (2013).

54. M. Kraft, Y. Luo, and J. B. Pendry, "Transformation optics: A time-and frequency-domain analysis of electron-energy loss spectroscopy," Nano Lett. **16**(8), 5156–5162 (2016).

55. J. B. Pendry, Y. Luo, and R. Zhao, "Transforming the optical landscape," Science **348**(6234), 521–524 (2015).

56. R. Q. Li, D. Hernángomez-Pérez, F. J. García-Vidal, and A. I. Fernández-Domínguez, "Transformation optics approach to plasmon-exciton strong coupling in nanocavities," Phys. Rev. Lett. **117**(10), 107401 (2016).

57. S. Yu and H. Ammari, "Hybridization of singular plasmons via transformation optics," Proc. Natl. Acad. Sci. **116**(28), 13785–13790 (2019).

58. J. B. Pendry, P. A. Huidobro, Y. Luo, and E. Galiff, "Compacted dimensions and singular plasmonic surfaces," Science **358**(6365), 915–917 (2017).

59. E. N Economou, "Surface plasmons in thin films," Phys. Rev. **182**(2), 539–554 (1969).

60. M. A. Miri, R. S. Duggan, and A. Alù, "Parity-Time Symmetry in Scattering Problems," In *Parity-time Symmetry and Its Applications*, D. Christodoulides and J. Yang, eds. (Springer, 2018)

61. A. Aubry and J. B. Pendry, "Transformation optics for plasmonics," in *Active Plasmonics and Tuneable Plasmonic Metamaterials*, A. V. Zayats and S. A. Maier, eds. (Wiley, 2013).

62. J. B. Pendry, "Negative refraction makes a perfect lens," Phys. Rev. Lett. **85**(18), 3966–3969 (2000).

63. B. Prade, J. Y. Vinet, and A. Mysyrowicz, "Guided optical waves in planar heterostructures with negative dielectric constant," Phys. Rev. B **44**(24), 13556–13572 (1991).

64. A. Aubry, D. Y. Lei, S. A. Maier, and J. B. Pendry, "Conformal transformation applied to plasmonics beyond the quasistatic limit," Phys. Rev. B **82**(20), 205109 (2010).

65. E. J. Zeman and G. C. Schatz, "An accurate electromagnetic theory study of surface enhancement factors for silver, gold, copper, lithium, sodium, aluminum, gallium, indium, zinc, and cadmium," J. Phys. Chem. **91**(3), 634–643 (1987).

66. A. Abdrabou and Y. Y. Lu, "Exceptional points for resonant states on parallel circular dielectric cylinders," J. Opt. Soc. Am. B **36**(6), 1659–1667 (2019).